Total-energy method based on the exact muffin-tin orbitals theory

L. Vitos
Applied Materials Physics, Department of Materials Science and Engineering, Royal Institute of Technology, SE-10044 Stockholm, Sweden

(Received 19 January 2001; published 14 June 2001)

I present a total-energy method based on the exact muffin-tin orbitals (EMTO) theory and the full charge density (FCD) technique. The FCD-EMTO method combines the accuracy of the full-potential method and the efficiency of the muffin-tin potential method. The one-electron Kohn-Sham equations are solved exactly for the overlapping muffin-tin potential and from the self-consistent solutions the full charge density is constructed. The EMTO kinetic energy, combined with the Coulomb and exchange-correlation terms calculated from the total density, yields the FCD-EMTO total energy. The accuracy of the FCD-EMTO method is demonstrated through several test calculations.

DOI: 10.1103/PhysRevB.64.014107 PACS number(s): 71.15.Nc, 71.20.Be, 71.20.Gj

I. INTRODUCTION

Attempts to develop new total energy calculation methods based on the density functional theory[1,2] and to improve on the existing ones have been amongst the most challenging campaigns of the computational materials science.[3–15] During the last decade the very efficient and widespread muffin-tin or atomic sphere approximation related methods have been overshadowed by the more accurate, and at the same time more demanding full-potential techniques. According to the density functional theory,[1] any reasonably accurate trial density is suitable to determine the total energy of the system within an error which is second order in the error of the charge density. This positiveness has been recognized by several groups of researchers[14–19] and it led to the elaboration of the full charge density (FCD) technique[14,15] as an alternative to the full-potential methods. The FCD technique was designed to maintain the efficiency of the muffin-tin methods and give total energies with the accuracy of the full-potential methods. Though, the original implementation of this technique,[20,21] in connection with the linear muffin-tin orbitals (LMTO) method,[7,22] proved highly promising in the case of close packed metals,[20,21] for systems of low symmetry it had serious shortcomings due to the inappropriate treatment of the kinetic energy term.[14] In order to increase the accuracy different corrections had to be included[14,22–25] and, therefore, the FCD-LMTO method loses its efficiency.

In the framework of the recently developed exact muffin-tin orbitals (EMTO) theory[3–5] the one-electron states, and consequently the one-electron kinetic energies, are calculated exactly for the muffin-tin potential. Within this formalism, in contrast to the usual muffin-tin based KKR (Korringa-Kohn-Rostoker) methods,[17,26] large overlapping potential spheres can be used for accurate representation of the exact one-electron potential.[4,27] Therefore, the EMTO theory provides an ideal ground for developing an accurate and efficient FCD based method.

In the present paper, starting from the self-consistent implementation of the EMTO theory[28] I put forward the FCD-EMTO total energy calculation method. In Sec. II I review the EMTO theory,[3,4] and the FCD technique.[14,15] In Sec. III some important details of the self-consistent procedure and of the total energy calculation technique are discussed. Finally, I establish the accuracy of the FCD-EMTO method by performing test calculations for some systems where reliable full-potential and experimental data are available.

II. THE FCD-EMTO METHOD

The self-consistent solution of the one-electron Kohn-Sham equations[2] involves two main problems: (i) the solution of the Schrödinger equation for the effective potential and (ii) the solution of the Poisson equation for the total electronic and protonic charge densities. In this section I explicate these two problems within the context of the EMTO formalism, and I give a short overview of the FCD technique.

A. The one-electron equations

In the EMTO theory[3–5] the one-electron Kohn-Sham equations

$$[-\nabla^2+v(\mathbf{r})]\Psi_j(\mathbf{r})=\epsilon_j\Psi_j(\mathbf{r}), \tag{1}$$

are solved within the muffin-tin approximation for the effective potential

$$v(\mathbf{r})\approx v_{mt}(\mathbf{r})\equiv v_0+\sum_R\,[v_R(r_R)-v_0], \tag{2}$$

where R runs over the lattice sites, $v_R(r_R)$ are spherical potentials, which become equal to v_0 outside the potential spheres of radii s_R. For accurate representation of the full potential these s spheres should overlap.[4,27] Here and in the following $\mathbf{r}_R\equiv\mathbf{r}-\mathbf{R}$, and throughout in the paper the atomic Ry units are used.

In order to solve the Schrödinger equation (1) for the muffin-tin potential (2) the wave function is expanded in terms of a complete basis set

$$\Psi_j(\mathbf{r})=\sum_{RL}\,\overline{\psi}^a_{RL}(\epsilon_j,\mathbf{r}_R)v^a_{RL,j}, \tag{3}$$

where L stands for (l,m), and $\overline{\psi}^a_{RL}$ are the muffin-tin orbitals defined for each site $\mathbf{R}$. In Eq. (3) the l summation usually includes terms up to $l_{\max}=3$, i.e., the s,p,d and f orbitals. The coefficients $v^a_{RL,j}$ are determined from the condition that the expansion (3) should be solution of Eq. (1) in the entire space. This condition leads to the kink cancellation or screened KKR equation.[17,26]

In the interstitial region, where the potential is approximated by v_0, it is customary to use as basis functions the solutions of the wave equation

$$[\nabla^2+\kappa^2]\psi^a_{RL}(\kappa,\mathbf{r}_R)=0, \quad \text{where} \quad \kappa^2\equiv\epsilon-v_0. \tag{4}$$

Within the EMTO formalism the $\psi^a_{RL}(\kappa,\mathbf{r}_R)$ functions are referred to as the screened spherical waves.[3] The boundary conditions for Eq. (4) are given in conjunction with nonoverlapping spheres centered at all sites $\mathbf{R}$ with radii a_R. The screened spherical waves on their own a spheres behave as a pure spherical harmonic $Y_L(\hat{r}_R)$, while the $Y_{L'}(\hat{r}_{R'})$ projections on all the other a spheres, i.e., for $R'\neq R$, vanish.[3] With these energy independent boundary conditions for κ^2 below the bottom of the $a-$spheres continuum, the screened spherical waves have short range and week energy dependence.[3] They form a complete basis set in the a-interstitial region and may be expanded in spherical harmonics $Y_{L'}(\hat{r}_{R'})$ around any site $\mathbf{R}'$, as

$$\psi^a_{RL}(\kappa,\mathbf{r}_R)=f^a_{Rl}(\kappa,r_R)Y_L(\hat{r}_R)\delta_{RR'}\delta_{LL'}+\sum_{L'} g^a_{R'l'}(\kappa,r_{R'}) \times Y_{L'}(\hat{r}_{R'})S^a_{R'L'RL}(\kappa), \tag{5}$$

where $f^a_{Rl}(\kappa,r_R)$ and $g^a_{Rl}(\kappa,r_R)$ are linear combinations[28] of spherical Bessel, $j_l(\kappa r_R)$, and Neumann, $n_l(\kappa r_R)$, functions.[29] The expansion coefficients, $S^a_{R'L'RL}(\kappa)$, are the elements of the *slope matrix*, which is related to the bare KKR structure constant matrix through the inhomogeneous Dyson equation[3]

$$S^a_{R'L'RL}(\kappa)=\mathcal{D}\{j_l(\kappa a_R)\}-\frac{1}{a_{R'}j_{l'}(\kappa a_{R'})} \times\left[-B(\kappa)+\kappa\frac{n(\kappa a)}{j(\kappa a)}\right]^{-1}_{R'L'RL}\frac{1}{j_l(\kappa a_R)},$$

where $\mathcal{D}$ denotes the logarithmic derivative, i.e., $\mathcal{D}\{j_l(r)\}\equiv r[\partial j_l(r)/\partial r]/j_l(r)$. The bare KKR structure constants are defined as the expansion coefficients of the $\kappa n_L(\kappa,\mathbf{r}_R)\equiv\kappa n_l(\kappa r_R)Y_L(\hat{r}_R)$ functions around site R' in terms of the $j_{L'}(\kappa,\mathbf{r}_{R'})\equiv j_{l'}(\kappa r_{R'})Y_{L'}(\hat{r}_{R'})$ functions, i.e. $\kappa n_L(\kappa,\mathbf{r}_R)=\Sigma_{L'}j_{L'}(\kappa,\mathbf{r}_{R'})B_{R'L'RL}(\kappa)$, with

$$B_{R'L'RL}(\kappa)\equiv 4\pi\sum_{L''} C^{L''}_{LL'}i^{-l+l'-l''}\kappa n_{L''}(\kappa,\mathbf{R}'-\mathbf{R}),$$

and where $C^{L''}_{LL'}$ are the real harmonic Gaunt coefficients.

In Eq. (5) $l\leqslant l_{\max}$, and the l' summation is infinite, which in practice is truncated at $l^h_{\max}\approx 8-12$. Terms with $l_{\max}<l'\leqslant l^h_{\max}$ are called ''highers.'' For $l\leqslant l_{\max}$ the $f^a_{Rl}(\kappa,r_R)$ and $g^a_{R'l'}(\kappa,r_{R'})$ functions satisfy the following boundary conditions at the a-spheres: $f^a(a)=1,\partial f(a)/\partial r=0,g^a(a)=0$, and $\partial g^a(a)/\partial r=1/a$, where for simplicity the indices have been omitted. For $l'>l_{\max}$ the tail function reduces to the Bessel function, i.e., $g^a_{R'l'}(\kappa,r_{R'})=-j_l(\kappa r_{R'})$. The screened spherical waves have no pure (lm) character,[30] and they are irregular at the origin.

For spherically symmetric potentials $v_R(r_R)$, i.e., close to the lattice sites, the basis functions are chosen to have pure (lm) character, and the radial parts are the regular solutions of the radial Schrödinger equation

$$\frac{\partial^2[r_R\phi_{Rl}(\epsilon,r_R)]}{\partial r_R^2}=\left[\frac{l(l+1)}{r_R^2}+v_R(r_R)-\epsilon\right]r_R\phi_{Rl}(\epsilon,r_R). \tag{6}$$

The partial waves, $\phi_{Rl}(\epsilon,r_R)$, are defined for any real or complex energy ϵ. Because a screened spherical wave behaves as $Y_L(\hat{r}_R)$ only on its own a sphere, the matching condition between $\psi^a_{RL}(\kappa,\mathbf{r}_R)$ and $\phi_{Rl}(\epsilon,r_R)Y_L(\hat{r}_R)$ should be set up at this sphere. The connection onto the potential sphere, which is usually larger than the a sphere, is done by introducing a free electron solution from the potential sphere back to the a sphere, which joins continuously and differentiable to the partial wave at s_R and continuously to the screened spherical wave at a_R. The radial part of the backwards extrapolated free-electron solution can be written in the form[3]

$$\varphi^a_{Rl}(\epsilon,r)=f^a_{Rl}(\kappa,r)+g^a_{Rl}(\kappa,r)D^a_{Rl}(\epsilon),$$

where $D^a_{Rl}(\epsilon)\equiv\mathcal{D}\{\varphi^a_{Rl}(\epsilon,a_R)\}$ is the logarithmic derivative of $\varphi^a_{Rl}(\epsilon,r)$ calculated at the a sphere. The exact muffin-tin orbitals are constructed as the superposition of the three basis functions, i.e.,

$$\overline{\psi}^a_{RL}(\epsilon,\mathbf{r}_R)=\psi^a_{RL}(\kappa,\mathbf{r}_R)+N^a_{Rl}(\epsilon)\phi_{Rl}(\epsilon,r_R)Y_L(\hat{r}_R) -\varphi^a_{Rl}(\epsilon,r_R)Y_L(\hat{r}_R), \tag{7}$$

where the last two terms are truncated outside the s spheres. The normalization function, $N^a_{Rl}(\epsilon)$, and the logarithmic derivative, $D^a_{Rl}(\epsilon)$, are determined from the matching condition between $\phi_{RL}(\epsilon,r_R)$ and $\varphi^a_{RL}(\epsilon,r_R)$ at $r_R=s_R$[28], viz.,

$$\frac{1}{N^a_{Rl}(\epsilon)}=\frac{\phi_{Rl}(\epsilon,s_R)}{f^a_{Rl}(\kappa,s_R)}\frac{\mathcal{D}\{\phi_{Rl}(\epsilon,s_R)\}-\mathcal{D}\{g^a_{Rl}(\kappa,s_R)\}}{\mathcal{D}\{f^a_{Rl}(\kappa,s_R)\}-\mathcal{D}\{g^a_{Rl}(\kappa,s_R)\}}$$

and

$$D^a_{Rl}(\epsilon)=-\frac{f^a_{Rl}(\kappa,s_R)}{g^a_{Rl}(\kappa,s_R)}\frac{\mathcal{D}\{\phi_{Rl}(\epsilon,s_R)\}-\mathcal{D}\{f^a_{Rl}(\kappa,s_R)\}}{\mathcal{D}\{\phi_{Rl}(\epsilon,s_R)\}-\mathcal{D}\{g^a_{Rl}(\kappa,s_R)\}}.$$

Using the exact muffin-tin orbitals (7) the wave function (3) will be a solution of Eqs. (1) and (2), if inside the s spheres the $l\leqslant l_{\max}$ components of the screened spherical waves,

multiplied by the expansion coefficients, are cancelled exactly by $\varphi^a_{Rl}(\epsilon,r_R)Y_L(\hat{r}_R)v^a_{RL,j}$, i.e., if the *kink cancellation* equation

$$\sum_{RL} K^a_{R'L'RL}(\epsilon_j)v^a_{RL,j} \equiv \sum_{RL} a_{R'}[S^a_{R'L'RL}(\kappa_j) - \delta_{R'R}\delta_{L'L}D^a_{Rl}(\epsilon_j)]v^a_{RL,j}=0, \tag{8}$$

is satisfied for all R' and $l' \leqslant l_{\max}$. Here and in the following $\kappa_j^2 \equiv \epsilon_j - v_0$. For energies ϵ_j, for which Eq. (8) is fulfilled, the wave function inside the potential sphere at **R** reduces to

$$\Psi_j(\mathbf{r}_R)=\sum_L N^a_{Rl}\phi_{Rl}(\epsilon_j,r_R)Y_L(\hat{r}_R)v^a_{RL,j} + \sum_{L'}^{l'>l_{\max}} g^a_{Rl'}(\kappa_j,r_R)Y_{L'}(\hat{r}_R) \times \sum_{R'L} S^a_{RL'R'L}(\kappa_j)v^a_{R'L,j}, \tag{9}$$

i.e., the $l'>l_{\max}$ components of $\psi^a_{RL}(\kappa_j,\mathbf{r}_R)$ penetrate into the spheres. However, for large l, due to the centrifugal term in the radial Schrödinger equation (6), the partial waves tend towards Bessel functions, i.e. towards the second term from the right hand side of Eq. (9).

The solutions of Eq. (8) are the one-electron energies and wave functions. Alternatively, these solutions may be obtained from the poles of the path operator $g^a_{R'L'RL}(z)$ defined for a complex energy z by

$$\sum_{R''L''} K^a_{R'L'R''L''}(z)g^a_{R''L''RL}(z)=\delta_{R'R}\delta_{L'L}.$$

Using the residue theorem and the expression of the overlap matrix of the exact muffin-tin orbitals[3]

$$\int \overline{\psi}^*_{R'L'}(z,\mathbf{r})\overline{\psi}_{RL}(z,\mathbf{r})d\mathbf{r}=\dot{K}^a_{R'L'RL}(z), \tag{10}$$

where the *over dot* denotes the energy derivative, the total number of states below the Fermi energy ϵ_F can be obtained as

$$N(\epsilon_F)=\frac{1}{2\pi i}\oint_{\epsilon_F} G(z)dz, \tag{11}$$

where

$$G(z)\equiv \sum_{R'L'RL} g^a_{R'L'RL}(z)\dot{K}^a_{RLR'L'}(z) - \sum_{RL}\left(\frac{\dot{D}^a_{Rl}(z)}{D^a_{Rl}(z)} - \sum_{\epsilon^D_{Rl}}\frac{1}{z-\epsilon^D_{Rl}}\right), \tag{12}$$

with $l,l' \leqslant l_{\max}$. The energy integral from Eq. (11) is performed on a complex contour that cuts the real axis below the bottom of the valence band and at ϵ_F. The first term from the right hand side of Eq. (12) may include the unphysical poles of $\dot{D}^a_{Rl}(z)$, which, however, are cancelled by the second term. ϵ^D_{Rl} denote the zeros of the logarithmic derivative function, $D^a_{Rl}(\epsilon)$. Note that the second term from the right hand side of Eq. (12) gives no contribution if $\dot{D}^a_{Rl}(z)$ is analytic function of z inside the complex energy contour.

In Eq. (10) the negligible terms due to the overlap between potential spheres have been omitted.[4] Aside from these terms, $N(\epsilon_F)$ gives the exact number of states at the Fermi level for the muffin-tin potential (2).

B. The full charge density

The electron density is given in terms of Kohn-Sham one-electron wave functions[2]

$$n(\mathbf{r})=\sum_j^{\epsilon_j\leqslant\epsilon_F} |\Psi_j(\mathbf{r})|^2,$$

where the summation includes the states below the Fermi level. From the expansion (3) of $\Psi_j(\mathbf{r})$ one obtains a multicenter form for the charge density, which, according to Eq. (9), can be transformed into one-center form around each site, i.e.,

$$n(\mathbf{r})=\sum_R n_R(\mathbf{r}_R)=\sum_{RL} n_{RL}(r_R)Y_L(\hat{r}_R). \tag{13}$$

Inside the Wigner-Seitz cell at **R** the partial components of the charge density $n_R(\mathbf{r}_R)$ can be expressed as

$$n_{RL}(r_R)=\frac{1}{2\pi i}\oint_{\epsilon_F}\sum_{L''L'} C^L_{L''L'}Z^a_{Rl''}(z,r_R)\tilde{g}^a_{RL''RL'}(z) \times Z^a_{Rl'}(z,r_R)dz, \tag{14}$$

where the l'' and l' summations include the *higher* terms as well. In Eq. (14) the following notations have been introduced:

$$Z^a_{Rl}(z,r_R)=\begin{cases} N^a_{Rl}(z)\phi_{Rl}(z,r_R) & \text{if } l\leqslant l_{\max} \text{ and } r_R\leqslant s_R,\\ \varphi^a_{Rl}(z,r_R) & \text{if } l\leqslant l_{\max} \text{ and } r_R>s_R,\\ -j_l(\kappa r_R) & \text{if } l>l_{\max} \text{ for all } r_R \end{cases}$$

and

$$\tilde{g}^a_{RL'RL}(z)\equiv\begin{cases} g^a_{RL'RL}(z)+\dfrac{\delta_{L'L}}{a_R\dot{D}^a_{Rl}(z)}\left(\dfrac{\dot{D}^a_{Rl}(z)}{D^a_{Rl}(z)}-\sum\limits_{\epsilon^D_{Rl}}\dfrac{1}{z-\epsilon^D_{Rl}}\right) & \text{if } l,l'\leqslant l_{\max}, \\ \sum\limits_{R''L''} g^a_{RL'R''L''}(z)S^a_{R''L''RL}(\kappa) & \text{if } l'\leqslant l_{\max} \text{ and } l>l_{\max}, \\ \sum\limits_{R''L''R'''L'''} S^a_{RL'R''L''}(\kappa)g^a_{R''L''R'''L'''}(z)S^a_{R'''L'''RL}(\kappa) & \text{if } l',l>l_{\max}. \end{cases}$$

In the last two equations $\kappa^2\equiv z-v_0$. The high-low and the low-high sub-blocks of the slope matrix are calculated by the blowing-up technique.[31] The charge density computed from Eqs. (13) and (14) is normalized within the unit cell, and for reasonable large $l^h_{\max}$ it is continuous at the cell boundaries.

In the case of translation symmetry in Eq. (8) R and R' run over the atoms in the primitive cell only, and the slope matrix, the kink matrix, and the path operator depend on the Bloch vector $\mathbf{k}$ from the first Brillouin zone.

C. The one-electron potential

Equations (8), (11), and (14) constitute the basis of the method used to solve the Schrödinger equation (1). In order to perform a self-consistent calculation one constructs the electron density from the solutions of the kink cancellation equation and calculates the new one-electron potential. Within the EMTO theory this latter procedure involves two consecutive steps:[32] the calculation of the full potential and the construction of the optimized overlapping muffin-tin wells. The first step, using the one-center formalism for the charge density and potential, is very demanding and it is inaccurate in the corners of the unit cell. However, within the spherical cell approximation (SCA),[28] employed in the present implementation of the EMTO theory, the overlapping muffin-tin potential depends only on the spherical part of the full-potential, which can be computed efficiently and with high accuracy.

In the SCA the Wigner-Seitz cells are substituted by spherical cells with volumes equal to the volumes of the real cells. If Ω_R denotes the volume of the Wigner-Seitz cell centered at $\mathbf{R}$ then $\Omega_R=\Omega_{w_R}\equiv(4\pi/3)w_R^3$, where w_R is the atomic sphere radius.

The spherical symmetric potentials $v_R(r_R)$ have to be chosen in a way that, together with the parameter v_0, to give the best approximation to the full potential $v(\mathbf{r})$. The idea from Ref. 32 is to minimize the mean of the squared deviation between the left and the right hand side of Eq. (2). This leads to a set of integral or differential equations for $v_R(r_R)$ and v_0. In the nonoverlapping muffin-tins case the equation for $v_R(r_R)$ reduces to the well known expression

$$v_R(r_R)=\frac{1}{4\pi}\int v(\mathbf{r})d\hat{\mathbf{r}}_R, \tag{15}$$

and v_0 reduces to the muffin-tin zero, i.e., to the average of the full potential calculated in the interstitial region. For overlapping muffin tins the equation for $v_R(r_R)$ involves terms coming from the overlapping region, which give rise to kink of $v_R(r_R)$ when r_R touches other muffin-tin spheres.[32] Here, instead of solving this equation, I fix the $v_R(r_R)$ function to the spherical average of the full potential given by Eq. (15). In this case, using the SCA for the Wigner-Seitz cell, the parameter v_0 has the following simple expression:[32,28]

$$v_0=\sum_R\int_{s_R}^{w_R} r_R^2\left[\int v(\mathbf{r})d\hat{\mathbf{r}}_R\right]dr_R \Big/ \sum_R\,[4\pi(w_R^3-s_R^3)/3]. \tag{16}$$

Therefore, both of the $v_R(r_R)$ function and the v_0 parameter are given in terms of the spherical symmetric part of the full potential. The motivation of the present choice for $v_R(r_R)$ is given in Sec. III B. In the following I show how $\int v(\mathbf{r})d\hat{\mathbf{r}}_R$ is computed within the FCD-EMTO method.

The electrostatic potential of the electronic $n(\mathbf{r})$ and protonic $Z_R\delta(r_R)$ charge densities, i.e.,

$$2\int\frac{n(\mathbf{r}')}{|\mathbf{r}-\mathbf{r}'|}d\mathbf{r}'-\sum_R\frac{2Z_R}{r_R},$$

can be divided into components due to the charges from inside and from outside of the potential sphere. The spherical symmetric part of the former component, calculated around site $\mathbf{R}$, can be obtained as

$$v^I_R(r_R)=8\pi\frac{1}{r_R}\int_0^{r_R} r_R'^2 n_{R(0,0)}(r_R')dr_R' + 8\pi\int_{r_R}^{s_R} r_R' n_{R(0,0)}(r_R')dr_R'-\frac{2Z_R}{r_R}. \tag{17}$$

The effect of charges from the outside of the potential sphere is taken into account by the usual Madelung potential, whose spherical symmetric part is given by

$$v^M_R=\frac{1}{w}\sum_{R'L'} M_{R(0,0)R'L'}Q^{\mathrm{SCA}}_{R'L'}, \tag{18}$$

where $M_{RLR'L'}$ are the elements of the Madelung matrix, w is the average atomic radius. The multipole moments Q^{SCA}_{RL} are calculated within the SCA

$$Q_{RL}^{\mathrm{SCA}}=\frac{\sqrt{4\pi}}{2l+1}\int_0^{w_R}\left(\frac{r_R}{w}\right)^l n_{RL}(r_R)r_R^2 dr_R - Z_R\delta_{L,(0,0)}+\delta^{\mathrm{SCA}}\delta_{L,(0,0)}. \quad (19)$$

Since the integral from Eq. (19) is performed over the spherical cell rather than over the unit cell, the monopole moments have to be renormalized within the unit cell.[28] The site independent constant δ^{SCA} is determined from the condition of charge neutrality.

The number of electrons inside the s sphere, denoted by $Q(s_R)$, is usually different from the number of electrons inside the cell $Q_{R(0,0)}^{\mathrm{SCA}}+Z_R$. This difference contributes with a constant shift Δv_R^M to the spherical potential. In the FCD-EMTO method this extra or missing charge is redistributed equally on the N_{NN} nearest neighbor cells, i.e.,

$$\Delta v_R^M=\frac{1}{w}\sum_{R_{\mathrm{NN}}} M_{R(0,0)R_{\mathrm{NN}}(0,0)}\Delta Q_{R_{\mathrm{NN}}}, \quad (20)$$

where $\Delta Q_{R_{\mathrm{NN}}}\equiv(1/N_{\mathrm{NN}})[Q_{R(0,0)}^{\mathrm{SCA}}+Z_R-Q(s_R)]$.

The total potential within the potential sphere is obtained as the sum of Eqs. (17), (18), and (20) and the spherical symmetric exchange-correlation potential, namely,

$$v_R(r_R)=v_R^I(r_R)+v_R^M+\Delta v_R^M+\mu_{xcR}(r_R). \quad (21)$$

If the spherical symmetric part of the exchange-correlation potential, calculated within the local density or a gradient level approximation, is approximated by $\mu_{xcR}[n_{R(0,0)}(r_R)]$ aside from the higher order multipole moments from Eq. (18), which in many cases can be neglected, all of the potential components from Eq (21) depend only on the spherical symmetric density $n_{R(0,0)}(r_R)$. Except the small approximations made in the Madelung terms, i.e., in Eqs. (18) and (20), the expression (21) gives the exact spherical part of the full potential inside the s sphere.

The best representation of the full potential by the overlapping muffin-tin potential can be achieved by choosing large overlapping spheres of radii s_R.[32] For an optimal choice of the potential spheres the potentials at s_R should be the same, i.e. $v_R(s_R)\approx$const for each R, and this const should have the maximum possible value for linear overlaps below 30-40 %.

D. The total energy functional

Within the FCD-EMTO method the kinetic energy is determined from the one-electron equations (1) as

$$T[n]=\frac{1}{2\pi i}\oint_{\epsilon_F} zG(z)dz-\sum_R\int_{\Omega_R} v_{mt}(\mathbf{r}_R)n_R(\mathbf{r}_R)d\mathbf{r}_R, \quad (22)$$

where the first term from the right hand side is the sum of the one-electron energies and $G(z)$ is given by Eq. (12). The second term is calculated within the unit cell and $v_{mt}(\mathbf{r})$ is the muffin-tin potential from Eq. (2).

The Coulomb and exchange-correlation parts of the total energy functional are calculated within the Wigner-Seitz cells using the shape function technique.[15,20,33] By means of the shape function, which is defined as *one* inside the cell and *zero* otherwise, any integral over the cell can be transformed into an integral over the sphere of radius w_R^c which circumscribes the cell. Consequently, the three dimensional (3D) Coulomb integrals reduce to one-dimensional (1D) integrals, which can be written in terms of

$$\tilde{n}_{RL}(r_R)=\sum_{L',L''} C_{L'L''}^L n_{RL'}(r_R)\sigma_{RL''}(r_R), \quad (23)$$

where $\sigma_{RL''}(r_R)$ are the partial components of the shape function.[15] In Eq. (23) the l'' summation is truncated at $l_{\max}^s$.

The total electrostatic contribution belonging to the cell at $\mathbf{R}$ is the sum of the intracell and intercell or Madelung energies. The intracell energy is given by

$$F_R^{\mathrm{intra}}[n_R]=\frac{\sqrt{4\pi}}{w}\sum_L\int_0^{w_R^c}\tilde{n}_{RL}(r_R)\left[\left(\frac{r_R}{w}\right)^l P_{RL}(r_R)+\left(\frac{r_R}{w}\right)^{-l-1} Q_{RL}(r_R)\right]r_R^2 dr_R, \quad (24)$$

where

$$P_{RL}(r_R)\equiv\frac{\sqrt{4\pi}}{2l+1}\int_{r_R}^{w_R^c}\tilde{n}_{RL}(r_R')\left(\frac{r_R'}{w}\right)^{-l-1}(r_R')^2 dr_R' \quad (25)$$

and

$$Q_{RL}(r_R)\equiv\frac{\sqrt{4\pi}}{2l+1}\int_0^{r_R}\tilde{n}_{RL}(r_R')\left(\frac{r_R'}{w}\right)^l(r_R')^2 dr_R'-\delta_{L,(0,0)}Z_R. \quad (26)$$

The intercell energy has the following form:[15,34]

$$F_R^{\mathrm{inter}}[n]=-\frac{1}{2w}\sum_L\sum_{R'\neq R}\frac{1}{2l+1}\left(\frac{b_{RR'}}{w}\right)^l Y_L(\widehat{\mathbf{b}_{RR'}}) \times\sum_{L',L''} Q_{RL'}\frac{4\pi(2l''-1)!!}{(2l-1)!!(2l'-1)!!}C_{L'L''}^L\delta_{l'',l+l'} \times\sum_{L'''} S_{RL'';\mathbf{R}'+\mathbf{b}_{RR'}L'''}Q_{R'L'''}, \quad (27)$$

where $S_{RL;R'L'}$ is the conventional LMTO structure constant and $Q_{RL}=Q_{RL}(w_R^c)$. The displacement vector $b_{RR'}$, introduced in Ref. 35, is proportional with the linear overlap of the circumscribed spheres to the cells at $\mathbf{R}$ and $\mathbf{R}'$. A reasonable choice for $b_{RR'}$ is described in Refs. 15,34.

The exchange-correlation energy belonging to the cell at $\mathbf{R}$ is calculated as the integral over the Wigner-Seitz cell of the exchange-correlation energy density $\epsilon_{\mathrm{xc}}[n(\mathbf{r})]$. For charge densities which deviate weakly from spherically symmetry the exchange-correlation energy density may be represented by a Taylor series around the spherically symmetric charge density,[14] and, therefore, the 3D integral can be reduced to 1D integral. However, for strongly anisotropic electron densities, like in the case of surfaces, the Taylor expan-

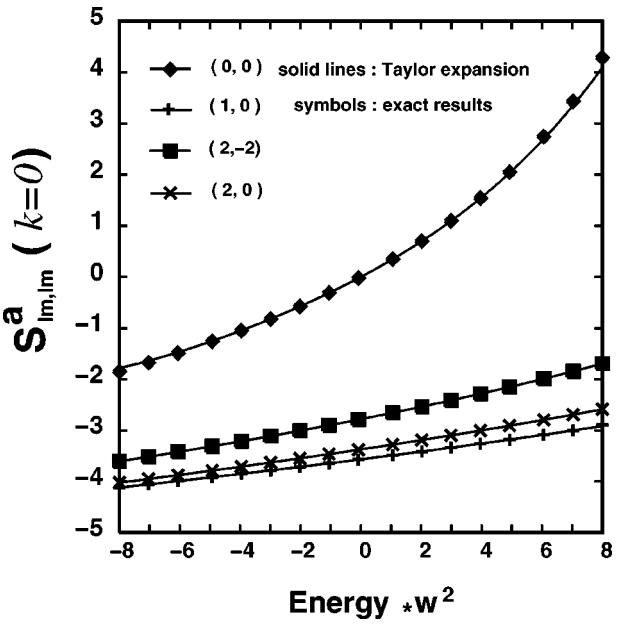

FIG. 1. The diagonal elements of the fcc slope matrix in the $\mathbf{k}=(0,0,0)$ point from the Brillouin zone versus $(\kappa w)^2$. The numbers in parenthesis denote the (l,m) quantum numbers. The Taylor expansion included terms up to the fourth order energy derivative.

sion is not convergent. In this case the exchange-correlation energy is evaluated by a direct 3D integration over the circumscribed sphere, i.e.,

$$E_{\mathrm{xc}R}[n]=\int_0^{2\pi}\int_0^{\pi}\int_0^{w_R^c}\epsilon_{xc}[n(\mathbf{r})]\sum_L^{l_{\max}^s}\sigma_{RL}(r_R)Y_L(\hat{\mathbf{r}}_R)r_R^2 dr_R \times\sin\theta d\theta d\phi. \tag{28}$$

III. DISCUSSION

A. Slope matrix

The screened spherical waves, for energies below the bottom of the a-sphere continuum, have short range and, therefore, the slope matrix can be calculated in real space. It was shown in Ref. 3 that the shortest range of the screened spherical waves can be achieved for nonoverlapping spheres with radii equal with $0.50-0.85w^i$, where w^i is the radius of inscribed or touching sphere, depending on the maximal orbital quantum number l of the partial waves explicitly included in the formalism.

In Fig. 1 I plotted the diagonal elements of the fcc slope matrix (symbols) calculated at the center of the Brillouin zone as a function of the dimensionless energy parameter $(\kappa w)^2$. For this test the real space calculation of $S^a(\kappa)$ was performed on five coordination shells plus the central site using the s,p, and d orbitals and $0.77w^i$ for the a-sphere radius. The figure demonstrates the weak and smooth energy dependence of the slope matrix up to $(\kappa w)^2\approx 6$. Therefore in the practical solution of the kink cancellation equation (8) the slope matrix can be estimated using a Taylor expansion around a fixed energy κ_0^2,

$$S^a_{R'L'RL}(\kappa)=S^a_{R'L'RL}(\kappa_0)+\frac{1}{1!}\dot{S}^a_{R'L'RL}(\kappa_0)(\kappa^2-\kappa_0^2)+\cdots. \tag{29}$$

The first and higher order energy derivatives are calculated analytically as described in Ref. 36. In Eq. (29) κ^2 is a complex energy not too far from κ_0^2. In Fig. 1 the solid lines were calculated with a fourth order expansion around $\kappa_0=0$. As one can observe, this expansion gives highly accurate energy dependence of the slope matrix over an energy range of approximately $(-8,+8)/w^2$ Ry around v_0. This energy window, usually, covers the whole occupied part of the valence electron spectra. However, in the case of semicore states laying far below the Fermi level, a second Taylor expansion around $\kappa_0^2\approx -20/w^2$ Ry is needed.

B. Optimized overlapping muffin-tin wells

In this section through a simple model potential I demonstrate how the full potential is represented by the overlapping muffin-tins, and I set out the advantages and shortcomings of the SCA used in Eq. (16). I model a general 3D full potential by a cosine potential in a simple cubic lattice, i.e.,

$$v_c(\mathbf{r})=-\cos\left(\frac{2\pi}{a}x\right)-\cos\left(\frac{2\pi}{a}y\right)-\cos\left(\frac{2\pi}{a}z\right)-3, \tag{30}$$

with the reference level in the corner of the Wigner-Seitz cell. For this potential, following the idea from Ref. 32, I minimize the mean of the squared deviation between the overlapping muffin tins and $v_c(\mathbf{r})$. The results obtained for potential sphere radii from $0.8a/2$ to $1.7a/2$ are shown in Fig. 2, where a denotes the cubic lattice constant. The three sets of results correspond to the following cases: (a) fully optimized overlapping muffin-tins calculated within the Wigner-Seitz cells (solid line), (b) fully optimized overlapping muffin-tins calculated within the spherical cells (dotted line), and (c) the spherical potential $v(r)$ fixed to the spherical part of the full potential and v_0 optimized for this $v(r)$ (dashed line), i.e., Eqs. (15) and (16).

In the upper panel of Fig. 2 I plotted the integrated local deviation of $v_c(\mathbf{r})$ and overlapping muffin tins. The percent error in the case of (a) decreases continuously, and around 30% linear overlap between the potential spheres it falls below half of the error observed for touching spheres. In the second case the error first decreases, at $\sim$15% overlap is starts to increase and at large overlaps it diverges. In the third case for overlapping s spheres there is a moderate improvement of the muffin-tin approach relative to the nonoverlapping situation, but above 30% overlap the integrated local deviation shows no significant dependence on the radius of the potential spheres.

The error in the one-electron energies, due to the overlap between the s spheres, is proportional[4] to the square of the muffin-tin discontinuity $[v(s)-v_0]$. This quantity is plotted in the middle panel of Fig. 2. With increasing overlap between the s spheres $[v(s)-v_0]$ converges smoothly to zero in the case of (a) and it diverges in the case of (b). When v_0 is calculated from Eq. (16), with $v(r)$ fixed to the spherical

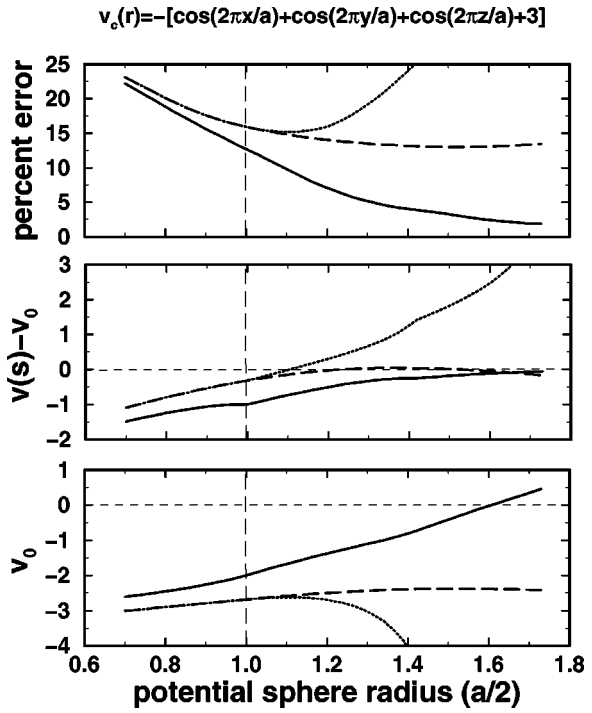

FIG. 2. Overlapping muffin-tin potential approximation to the cosine potential in cubic lattice (shown on the top of the figure, a denotes the lattice constant). Upper panel: integrated local deviation of the full-potential $[v_c(\mathbf{r})]$ and overlapping muffin-tins (in %). Middle panel: muffin-tin discontinuity (in arbitrary units). Lower panel: muffin-tin zero (relative to the zero potential level, in arbitrary units). Solid line: fully optimized overlapping muffin-tins calculated in the Wigner-Seitz cells; dotted line: fully optimized overlapping muffin-tins calculated in the spherical cells; dashed line: spherical potential fixed to the spherical part of the full-potential and muffin-tin zero optimized for this spherical potential, i.e., Eqs. (15) and (16). The radius corresponding to the touching spheres is marked by vertical lines.

part of the full potential $[v(s)-v_0]$ approaches zero already at small overlaps and it remains close to zero up to linear overlaps of 60–70 %. Consequently, in the third case the one-electron energies of monoatomic systems will depend negligible on the overlap between the potential spheres.[28]

In order to get well localized slope matrices for energies around the Fermi level, where $(\kappa_F w)^2=(\epsilon_F-v_0)w^2\gtrsim 5$, one prefers to have v_0 close to ϵ_F. For the cosine potential (30) v_0 is plotted in the lower part of Fig. 2. In the case of (a) v_0 increases with s and it reaches the zero potential level at $\sim$60% overlap. When the muffin-tins are fully optimized inside the spherical cell v_0 decreases with s for overlaps larger than $\sim$15%. In the third case v_0 increases slightly with the overlap but it always remains well bellow its optimal value, i.e., the one from the first case.

From these results one clearly sees that the accuracy of the overlapping muffin-tin approximation to the full potential, as far as the optimization is performed within the Wigner-Seitz cells, can be improved substantially by increasing the overlap between the potential spheres. However, using the spherical cell model, due to the improper description of the full potential, the fully optimized overlapping muffin-tin approximation breaks down for linear overlaps larger than 10–15 %. One possibility to overcome this problem is given by the third case (c), which is adopted in the present implementation of the EMTO method as well.

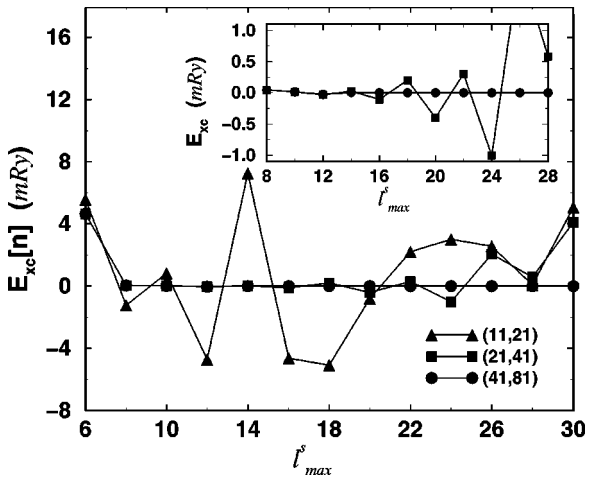

FIG. 3. Convergence test for the exchange-correlation energy of fcc Cu as function of the maximal l values used in Eq. (28). The energies are plotted relative to the converged result. The numbers in parenthesis denote the total number of θ and ϕ Gaussian mesh points on the spherical surface.

C. The $E_{xc}[n]$ energy term

The convergence properties of the electrostatic energy components presented in Sec. II D have been studied in details in Refs. 20,34. Here I discuss the convergence properties of the exchange-correlation energy term, calculated from Eq. (28). The surface integral over θ and ϕ is performed using the two dimensional (2D) Gaussian integration method. In Fig. 3 I plotted the exchange-correlation energy of fcc Cu, relative to its converged value, in terms of $l^s_{\max}$. Different symbols correspond to three different sets of 2D mesh points. It is seen that no convergence can be achieved for a small number of points ($N_\theta=11, N_\phi=21$). By doubling the number of 2D mesh points the converged value is recovered already for $l^s_{\max}=8-10$, but for $l^s_{\max}>16-18$ the energy starts to oscillate and it diverges. Only for very large number of mesh points the summation from Eq. (28) becomes absolutely convergent. This behavior is connected with the fact that for large l values, which are important for the proper mapping of the shape of the Wigner-Seitz cell, the spherical harmonics have more and more structure, and this can not be correctly described unless the surface integral is carried out with very high accuracy.

IV. APPLICATIONS

The FCD-EMTO total energy calculation method has been applied to different systems including bulk metals and semiconductors,[37,38] oxides,[39,40] monoatomic strings,[41] dimers,[37] etc. Here I present result obtained for bulk solids, monovacancies in fcc Al, and magnesium silicate perovskites. Through these examples I intend to demonstrate the

TABLE I. Theoretical equilibrium atomic radii (S in Bohr) and bulk moduli (B in GPa) for some selected solids. The present calculations have been performed for crystallographic α phases, and the results obtained by the full-potential linearized augmented plane-wave (LAPW) method and the experimental values are from Ref. 45. Δ_e and Δ_{LAPW} denote the mean absolute values of the relative deviations relative to the experimental values and to the LAPW results, respectively.

	FCD-EMTO				Full-potential				Experimental	
	S_{LDA}	S_{GGA}	B_{LDA}	B_{GGA}	S_{LDA}	S_{GGA}	B_{LDA}	B_{GGA}	S	B
Na	3.769	3.916	8.2	7.6	3.77	3.91	9.2	7.6	3.936	6.9
Al	2.947	2.989	81.2	75.2	2.94	2.98	84.0	77.3	2.991	77.3
Fe	2.565	2.645	253	178	2.56	2.64	259	198	2.667	172
Cu	2.602	2.684	193	137	2.60	2.68	191	139	2.658	138
Pd	2.846	2.916	235	184	2.84	2.91	226	174	2.873	181
W	2.929	2.977	312	292	2.92	2.96	335	298	2.940	310
Pt	2.888	2.943	304	244	2.88	2.93	312	247	2.892	283
Au	2.998	3.081	194	134	2.99	3.07	195	142	2.997	172
Si	3.163	3.198	100	92.8	3.17	3.21	97.0	89.0	3.182	98.8
Ge	3.303	3.384	71.6	61.2	3.30	3.38	71.2	59.9	3.318	76.8
GaAs	3.296	3.375	73.0	62.0	3.29	3.37	74.3	60.7	3.312	74.8
NaCl	3.202	3.346	32.9	23.0	3.21	3.34	32.2	23.4	3.306	24.5
Δ_e	1.48 %	1.28 %	17.2 %	9.2 %	1.63 %	1.19 %	19.1 %	9.9 %		
Δ_{LAPW}	0.20 %	0.27 %	3.3 %	3.3 %						

accuracy of the present method for simple and transition metals, semiconductors, strongly inhomogeneous densities occurring near the vacancies and in open structures, high pressure properties, etc. First I describe the most important numerical details and after I analyze the FCD-EMTO results comparing them to the available full-potential and experimental data.

A. Numerical details

The one-electron equations were solved within the scalar-relativistic approximations and the core states were recalculated after each iteration. In the EMTO basis set I included s,p, and d orbitals for simple metals, semiconductors and perovskites and s,p,d, and f orbitals for transition metals. For the exchange-correlation term I used the local density approximation (LDA) with the Perdew-Wang parametrization[42] of the results of Ceperley and Alder.[43] The kink matrix and path operator were calculated for $16-32$ complex energy points, depending on the system, and they were distributed exponentially on a semicircular contour. The k-point sampling was performed on a uniform grid in the Brillouin zone.

In the one-center expansion of the full charge density, Eq. (13), I including terms up to $l^h_{\mathrm{max}}=8$. The shape functions were generated for $l^s_{\mathrm{max}}=30$, and the functions $\tilde{n}_{RL}(r_R)$ with $l>l^s_{\mathrm{max}}$ were neglected. For Wigner-Seitz cells with nonoverlapping circumscribed spheres the displacement vector was set to zero, and the two remaining l'' and l''' summmations from Eq. (27) were truncated at $l^m_{\mathrm{max}}=8$. Using the full charge density, in addition to the LDA energy, I calculated the total energy within the generalized gradient approximation (GGA) (Ref. 44) as well.

The radii of the potential spheres, except in the case of magnesium silicate perovskites, were fixed to the radii of the atomic spheres, i.e. $s_R=w_R$. In the perovskites structures the overlap between the atomic spheres is 32–34 %, and the muffin-tin discontinuities vary between -0.13 and 0.11 Ry. In order to minimize the overlap error in the kinetic energy, I decreased the radii of the potential spheres around the oxygen atoms to $0.8w_O$. With this choice the largest linear overlap is around 19–20 %, and the error in the kinetic energy is of order of 1 μ Ry.

B. Equilibrium volumes and bulk moduli of solids

As a first test of the FCD-EMTO method I have calculated the atomic volumes and bulk moduli of several metals and semiconductors in their observed low temperature crystal structures. The results obtained within the LDA and GGA are presented in Table I, where, for comparison, I have included the full-potential[45] and experimental values as well. The full-potential calculation was performed with the linear augmented plane wave method[46] and it employed the same LDA and GGA exchange-correlation energy functionals as those from the present calculation. The mean deviations between the present atomic radii and bulk moduli and those of Ref. 45 are shown at the bottom of the table. The agreement between the two sets of data is very satisfactory. The closeness of the mean absolute relative differences in the LDA and GGA shows that the present method performs equally well for the local and nonlocal exchange-correlation functionals.

C. Vacancy formation energies

The vacancy in fcc Al has been used several times as a benchmark of the total energy calculation methods.[47–49] Us-

TABLE II. Theoretical (LDA) and experimental formation energies (E_v in eV) and the relaxation of the first nearest neighbors ($\delta_{\rm NN}$ in %) of a vacancy in fcc Al. The present calculations have been performed on 16 (numbers in parenthesis) and 32 atoms supercells.

	FCD-EMTO	Full-potential	Experimental
E_v, unrelaxed	0.84(0.89)	0.82 [a],0.73 [b]	
E_v, relaxed	0.66(0.64)	0.66, [a],0.62 [b],0.66 [c]	0.67 ± 0.03 [d]
δ_{NN}	$-1.41(-1.58)$	-1.50 [b]	

[a]Reference 47.
[b]Reference 49.
[c]Reference 48.
[d]Reference 55.

ing supercell geometries of 16 and 32 atoms I have calculated the formation energies of mono vacancies in Al and the results are listed in Table II. I found that increasing the size of the supercell beyond 32 atoms, as long as the proper convergence of the Brillouin zone sampling was ensured, had no significant effect on the formation energy. The present unrelaxed values were obtained for ideal fcc based supercells, while the relaxed values correspond to the radial relaxation of the nearest neighbors (NN) of the vacancy. The changes of the vacancy formation energies with the NN distances are shown in Fig. 4.

The unrelaxed and relaxed FCD-EMTO energies for 32 atoms supercell agree very well with the pseudopotential results from Refs. 47,48, but they are with 13 and 6 %, respectively, larger than those obtained using the full-potential KKR method.[49] This difference might be assigned to the fact that in Ref. 49 the relaxation of the potential beyond the nearest neighbors to the vacancy was neglected. The FCD-EMTO method gives a small inward relaxation of the NN lattice sites, in good accordance with the full-potential KKR results.[49]

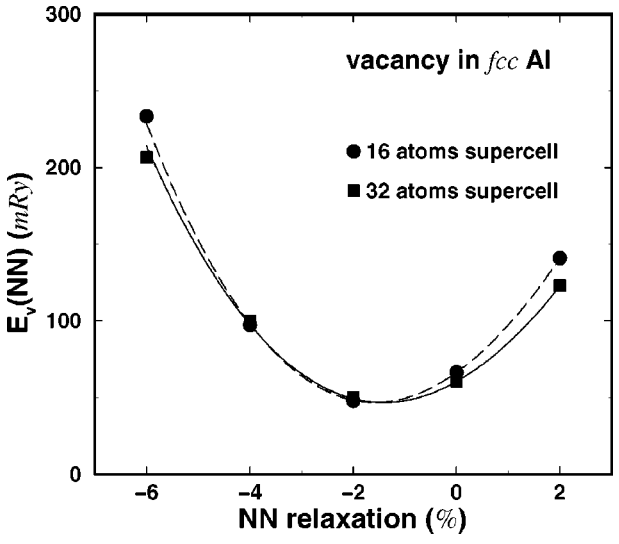

FIG. 4. Formation energies (in mRy) as functions of the nearest-neighbor (NN) distance of a vacancy in fcc Al. The energy minima correspond to -1.58 and -1.41 % inward relaxation of the first coordination shell around the vacancy in 16 and 32 atoms supercells, respectively.

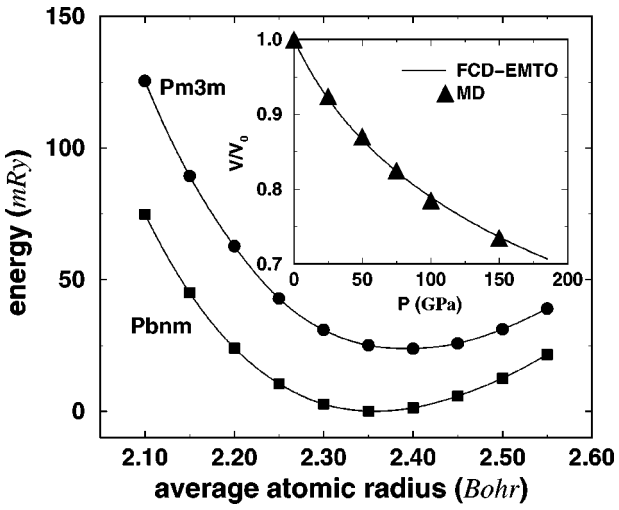

FIG. 5. Calculated total energies (per atom) of orthorhombic and cubic $MgSiO_3$ as functions of the average atomic radius. The energies are plotted relative to the orthorhombic ground state total energy. The symbols denote the results obtained with the FCD-EMTO method and the connecting line is a Morse-type fit (Ref. 54). In the insert the equation of state of orthorhombic phase is compared to the *ab initio* molecular dynamics calculation (Ref. 51).

D. Ground state properties of $MgSiO_3$ perovskites

The $MgSiO_3$ is the most abundant mineral of the Earth's lower mantle. The knowledge of the exact behavior of this perovskite under high pressures and temperatures is unavoidable in advanced seismic research. Here, using the FCD-EMTO method, I study the orthorhombic and cubic phases of $MgSiO_3$, and compare the present results with the available full-potential calculations.[50,51]

In the orthorhombic structure with $Pbnm$ symmetry the magnesium and four oxygen atoms occupy the $(4c)$ positions. The four silicon atoms are in the $(4b)$ positions, and the rest of the oxygen atoms are situated in the general $(8d)$ positions. The cubic perovskite structure has $Pm\bar{3}m$ symmetry and the Mg cation is situated in the center of the cube defined by eight corner sharing SiO_6 octahedra. According to high pressure and high-temperature measurements on silicate perovskite,[52] the orthorhombic distortion away from the cubic symmetry remains nearly constant with the pressure. Therefore, in the present study for each volume I used the experimental structural parameters from Ref. 53.

The FCD-EMTO total energies per atoms for $Pbnm$ and $Pm\bar{3}m$ phases as functions of the average atomic radii are plotted in Fig. 5. The equations of state were derived by fitting the energy versus volume curves to a Morse form.[54] In Table III the present zero pressure volumes, bulk moduli and structural energy difference are compared to the full-potential results from Refs. 50,51. The agreement between the theoretical results, in view of the fact the full-potential techniques have their own numerical approximations, may

TABLE III. Comparison of the theoretical (LDA) and experimental equilibrium atomic radii (S in Bohr), bulk moduli (B in GPa) and structural energy difference (ΔE in mRy/atom) of $MgSiO_3$ perovskite in orthorhombic ($Pbnm$) and cubic ($Pm\bar{3}m$) phases.

	FCD-EMTO			Full-potential			Experimental	
Structure	S	B	ΔE	S	B	ΔE	S	B
$Pbnm$	2.358	253		2.349 [a],2.333 [b]	266 [a],259 [b]		2.357 [b]	261 [b]
$Pm\bar{3}m$	2.394	258	23.3	2.381 [b]	258 [b]	20 [a],22.1 [b]		

[a]Reference 50.
[b]Reference 51.

be considered very satisfactory. It is seen from Fig. 5 that the stability of orthorhombic phase with respect to the cubic phase increases with the pressure from 23.3 mRy/atom at zero pressure to ~48 mRy/atom at 150 GPa. This observation compares well with the *ab initio* molecular dynamics (MD) results from Ref. 51, where at 150 GPa pressure an increase with ~30 mRy/atom, relative to the zero pressure value, of the stability of the $Pbnm$ phase with respect to the $Pm\bar{3}m$ phase was reported. In the insert of Fig. 5 I compare the present pressure-volume equation of state with the *ab initio* MD results.[51] The two sets of data are very close, and the slightly increasing deviation between them at large pressures might be assigned to the lattice relaxation neglected in the present study.

V. CONCLUSIONS

I have presented and tested a full charge density technique based on the exact muffin-tin orbitals theory. The EMTO kinetic energy, determined exactly for the optimized overlapping muffin-tin potential, is combined with the Coulomb and exchange-correlation energies calculated from the total charge density using the shape function technique. The FCD-EMTO method has been tested on different system, where the conventional methods based on *spherical approximations* fail, and the inclusion of correction terms into these methods is unavoidable. The general good agreement between the present total energy results and those obtained using full-potential techniques clearly demonstrates that the FCD-EMTO method has the accuracy of the full-potential techniques. Concerning the efficiency of the present implementation of the method, a self-consistent FCD-EMTO calculation needs about three times more computer time than the LMTO based FCD method.

ACKNOWLEDGMENTS

The author acknowledges the interesting and helpful discussions with Professor O. K. Andersen. The Swedish Natural Science Research Council, the Swedish Foundation for Strategic Research and Royal Swedish Academy of Sciences are acknowledged for financial support.

[1] P. Hohenberg and W. Kohn, Phys. Rev. **136**, B864 (1964).
[2] W. Kohn and L.J. Sham, Phys. Rev. **140**, A1133 (1965).
[3] O. K. Andersen, O. Jepsen, and G. Krier, in *Lectures on Methods of Electronic Structure Calculations*, edited by V. Kumar, O. K. Andersen, and A. Mookerjee (World Scientific Publishing, Singapore, 1994), pp. 63–124.
[4] O. K. Andersen, C. Arcangeli, R. W. Tank, T. Saha-Dasgupta, G. Krier, O. Jepsen, and I. Dasgupta, in *Tight-Binding Approach to Computational Materials Science*, edited by P. E. A. Turchi, A. Gonis, and L. Colombo, MRS Symposia Proceedings No. 491 (Materials Research Society, Pittsburgh, 1998), pp. 3–34.
[5] O. K. Andersen, T. Saha-Dasgupta, R. W. Tank, C. Arcangeli, O. Jepsen, and G. Krier, in *Electronic Structure and Physical Properties of Solids: The Uses of the LMTO Method*, edited by H. Dreyssé, Lectures Notes in Physics (Springer-Verlag, Berlin, 2000),
pp. 3–84.
[6] O. K. Andersen and T. Saha-Dasgupta, Phys. Rev. B **62**, R16 219 (2000).
[7] H.L. Skriver, *The LMTO Method* (Springer-Verlag, Berlin, 1984).
[8] R. Zeller, Phys. Rev. B **55**, 9400 (1997).
[9] T. Huhne, C. Zecha, H. Ebert, P. H. Dederichs, and R. Zeller, Phys. Rev. B **58**, 10 236 (1998).
[10] N. Papanikolaou, R. Zeller, P. H. Dederichs, and N. Stefanou, Phys. Rev. B **55**, 4157 (1997).
[11] J. M. Wills, O. Eriksson, M. Alouani, and D. L. Price, in *Electronic Structure and Physical Properties of Solids: The Uses of the LMTO Method* (Ref. 5), pp. 85–113.
[12] M. Methfessel, M. van Schilfgaarde, and R. A. Casali, in *Electronic Structure and Physical Properties of Solids: The Uses of the LMTO Method* (Ref. 5), pp. 85–113.
[13] I. A. Abrikosov, A. M. N. Niklasson, S. I. Simak, B. Johansson, A. V. Ruban, and H. L. Skriver, Phys. Rev. Lett. **76**, 4203 (1996).
[14] L. Vitos, J. Kollár, and H.L. Skriver, Phys. Rev. B **55**, 13 521 (1997).
[15] J. Kollár, L. Vitos, and H. L. Skriver, in *Electronic Structure and Physical Properties of Solids: The Uses of the LMTO Method* (Ref. 5), pp. 85–113.
[16] M. Asato, A. Settels, T. Hoshino, T. Asada, S. Blügel, R. Zeller,

and P. H. Dederichs, Phys. Rev. B **60**, 5202 (1999).
[17] O. K. Andersen, A.V. Postnikov, and S.Yu. Savrasov, in *Applications of Multiple Scattering Theory in Materials Science*, edited by W.H. Butler, P.H. Dederichs, A. Gonis, and R.L. Weaver (Materials Research Society, Pittsburgh, PA, 1992).
[18] O.C. Rodriguez and M. Methfessel, Phys. Rev. B **45**, 90 (1992).
[19] V.P. Antropov and B.N. Harmon, Phys. Rev. B **51**, 1918 (1995).
[20] L. Vitos, J. Kollár, and H. L. Skriver, Phys. Rev. B **49**, 16 694 (1994).
[21] J. Kollár, L. Vitos, and H. L. Skriver, Phys. Rev. B **49**, 11 288 (1994).
[22] O.K. Andersen, O. Jepsen, and M. Sob, in *Electronic Band Structure and its Applications*, edited by M. Yussouff (Springer, Berlin, 1987).
[23] L. Vitos, A. V. Ruban, H. L. Skriver, and J. Kollár, Surf. Sci. **411**, 186 (1998).
[24] L. Vitos, J. Kollár, and H. L. Skriver, Phys. Rev. B **55**, 4947 (1997).
[25] J. Kollár, L. Vitos, and H. L. Skriver, in *Actinides and the Environment*, Vol. 41 of NATO Advanced Studies Institute Series, edited by P. A. Sterne, A. Gonis, and A. A. Borovoi (Plenum, New York, 1998), p. 97.
[26] L. Szunyogh, B. Újfalussy, P. Weinberger, and J. Kollár, Phys. Rev. B **49**, 2721 (1994).
[27] C. Arcangeli, O.K. Andersen, and R.W. Tank (unpublished).
[28] L. Vitos, H.L. Skriver, B. Johansson, and J. Kollár, Comput. Mater. Sci. **18**, 24 (2000).
[29] *Handbook of Mathematical Functions*, edited by M. Abramowitz and I. A. Stegun (Dover, New York, 1970).
[30] A function $f_L(\mathbf{r})$ has pure (lm) character if the angular part is fully described by a real spherical harmonic, viz., if $f_L(\mathbf{r}) = f_L(r)Y_{lm}(\hat{\mathbf{r}})$.
[31] O. K. Andersen, O. Jepsen, and D. Glötzel, in *Highlights of Condensed-Matter Theory*, edited by F. Bassani, F. Fumi, and M. P. Tosi (North-Holland, New York, 1985).
[32] O. K. Andersen and C. Arcangeli (unpublished).
[33] B. Drittler, M. Weinert, R. Zeller, and P. H. Dederichs, Solid State Commun. **79**, 31 (1991).
[34] L. Vitos and J. Kollár, Phys. Rev. B **51**, 4074 (1995).
[35] A. Gonis, E. C. Sowa, and P. A. Sterne, Phys. Rev. Lett. **66**, 2207 (1991).
[36] R. Tank, C. Arcangeli, and O. K. Andersen (unpublished).
[37] L. Vitos, B. Johansson, J. Kollár, and H. L. Skriver, Phys. Rev. B **62**, 10 046 (2000).
[38] L. Vitos, B. Johansson, and J. Kollár, Phys. Rev. B **62**, R11 957 (2000).
[39] B. Magyari-Köpe, L. Vitos, and J. Kollár, Phys. Rev. B **63**, 104111 (2001).
[40] A. Landa (unpublished).
[41] A. V. Ruban (unpublished).
[42] J. Perdew and Y. Wang, Phys. Rev. B **45**, 13 244 (1992).
[43] D.M. Ceperley and B.J. Alder, Phys. Rev. Lett. **45**, 566 (1980).
[44] J.P. Perdew, K. Burke, and M. Ernzerhof, Phys. Rev. Lett. **77**, 3865 (1996).
[45] S. Kurth, J. P. Perdew, and P. Blaha, Int. J. Quantum Chem. **75**, 889 (1999).
[46] P. Blaha, K. Schwarz, P. Sorantin, and S. B. Trickey, Comput. Phys. Commun. **59**, 399 (1990).
[47] N. Chetty, M. Weinert, T. S. Rahman, and J. W. Davenport, Phys. Rev. B **52**, 6313 (1995).
[48] D. E. Turner, Z. Z. Zhu, C. T. Chan, and K. M. Ho, Phys. Rev. B **55**, 13 842 (1997).
[49] T. Hoshino, N. Papanikolaou, R. Zeller, P. H. Dederichs, M. Asato, T. Asada, and N. Stefanou, Comput. Mater. Sci. **14**, 56 (1999).
[50] L. Stixrude and R.E. Cohen, Nature (London) **364**, 613 (1993).
[51] R. M. Wentzcovitch, J. L. Martins, and G. D. Price, Phys. Rev. Lett. **70**, 3947 (1993).
[52] E. Knittle and R. Jeanloz, Science **235**, 668 (1987).
[53] H. Horiuchi, E. Ito, and D. J. Weidner, Am. Mineral. **72**, 357 (1987).
[54] V.L. Moruzzi, J.F. Janak, and K. Schwarz, Phys. Rev. B **37**, 790 (1988).
[55] P. Ehrhart, P. Jung, H. Schulta, and H. Ullmaier, in *Atomic Defects in Metals*, edited by H. Ullmaier, Landolt-Bornstein New Series, Group III, Vol. 25 (Springer-Verlag, Berlin, 1990).